Structure and Variability of Internal Tides in Luzon Strait*

ANDY PICKERING,[+,##] MATTHEW ALFORD,[+,#,@@] JONATHAN NASH,[@] LUC RAINVILLE,[&]
MAARTEN BUIJSMAN,[**] DONG SHAN KO,[++] AND BYUNGHO LIM[@]

[+] *Applied Physics Laboratory, and School of Oceanography, University of Washington, Seattle, Washington*
[#] *Scripps Institution of Oceanography, La Jolla, California*
[@] *Oregon State University, Corvallis, Oregon*
[&] *Applied Physics Laboratory, University of Washington, Seattle, Washington*
[**] *Department of Marine Science, University of Southern Mississippi, Stennis Space Center, Mississippi*
[++] *Oceanography Division, Naval Research Laboratory, Stennis Space Center, Mississippi*

ABSTRACT

The Luzon Strait is the generation region for strong internal tides that radiate westward into the South China Sea and eastward into the western Pacific. Intrusions of the Kuroshio and strong mesoscale variability in the Luzon Strait can influence their generation and propagation. Here, the authors use eight moorings and two numerical models to investigate these relationships by quantifying the coherence of the diurnal and semidiurnal internal tides in the Luzon Strait. This study finds that the level of coherence of internal tide generation, energy, and energy flux is quite variable, depending on the specific location within the Luzon Strait. Large-scale spatial patterns in internal tide pressure and velocity exist across the region, shaped by the bathymetry, mean flow, and stratification. Internal tide coherence is lower (<30%) near large gradients in this pattern (predominantly along the eastern ridge), which are shifted by the variable Kuroshio and mesoscale fields. At other locations within the Luzon Strait, the internal tide is largely coherent (>80%), and simple calculations suggest that remote sources of internal tides could account for these small decreases in coherence. To the west of the Luzon Strait (away from the primary generation regions), the model suggests that diurnal internal tide energy is more coherent than semidiurnal.

1. Introduction

Internal tides, generated where the barotropic tides force stratified water over underwater bathymetry, are thought to provide a significant fraction of the 2 TW of energy required to maintain abyssal stratification and the meridional overturning circulation (Munk and Wunsch 1998). They contribute to ocean mixing through a cascade of energy to smaller-scale waves or by shoaling on remote continental slopes. A better understanding of the generation, propagation, and dissipation of internal tides near major generation sites is necessary to understand and predict these processes under present and future oceanographic conditions.

One large source of internal tides is the Luzon Strait (Simmons et al. 2004; Jan et al. 2008), where internal tides are generated at two steep submarine ridges separating the South China Sea (SCS) from the Pacific Ocean (Fig. 1). In addition to the complex bathymetry, the Luzon Strait also features intrusions of the Kuroshio and high mesoscale variability. The Internal Waves in Straits Experiment (IWISE) is a multi-investigator initiative funded through the Office of Naval Research to investigate internal wave dynamics in this complex environment using a combination of shipboard campaigns and moored observations (Alford et al. 2015). Two major scientific objectives of IWISE are determining how internal tides in the Luzon Strait are affected by 1) a double-ridge system with

Corresponding author address: Andy Pickering, College of Earth, Ocean, and Atmospheric Sciences, Oregon State University, 442 Burt Hall, Corvallis, OR 97331.
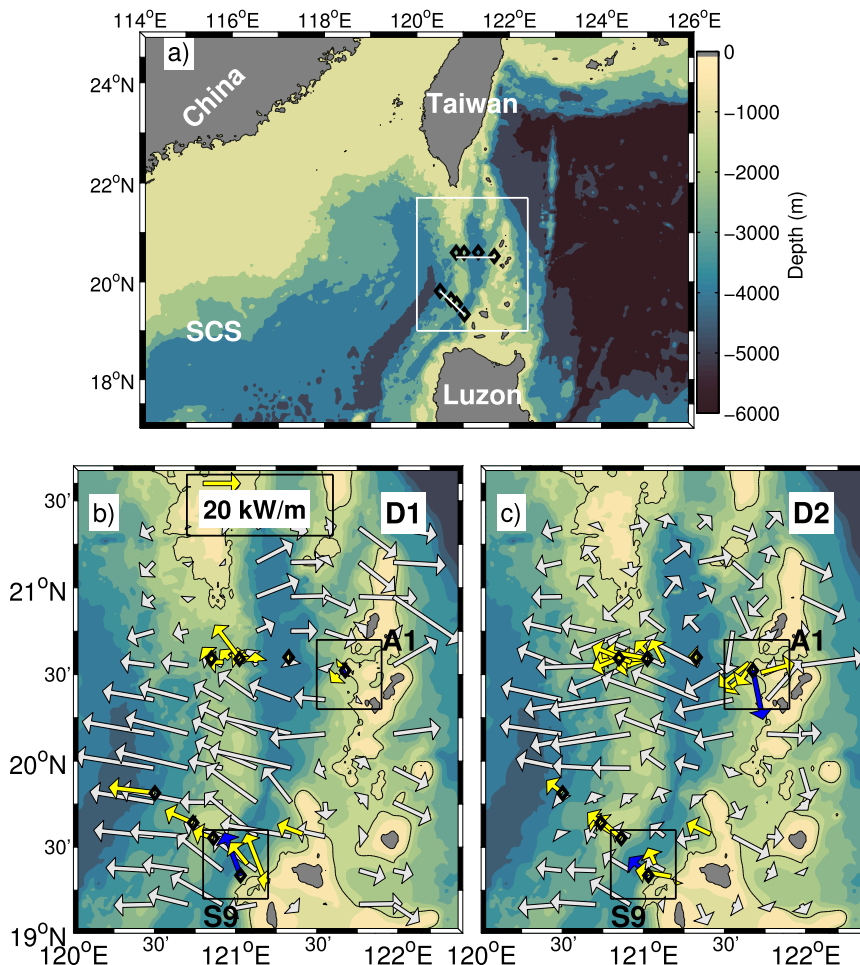E-mail: andypicke@gmail.com

FIG. 1. (a) Map of larger region, including SCS. White box indicates region shown in lower panels. Black diamonds indicate locations of the eight moorings deployed during summer 2011. White lines through moorings indicate the northern and southern lines referred to in the text. Map of the Luzon Strait with mooring locations and depth-integrated (b) diurnal (D1) and (c) semidiurnal (D2) energy fluxes. Modeled MITgcm energy fluxes are shown in white. Fluxes measured from LADCP/CTD stations are shown in yellow. Time-mean fluxes from moorings A1 and S9 are shown in blue. Boxes around these moorings indicate regions shown in Fig. 10. The 1000-m isobath is contoured.

complex topography and 2) strong, time-variable currents and stratification.

As it propagates west from the ridges, the internal tide often steepens into nonlinear internal waves (NLIWs) (Ramp et al. 2004; Farmer et al. 2009; Li and Farmer 2011; Lien et al. 2014) that are associated with large vertical displacements, currents, and turbulence that may impact the local ecosystem (Wang et al. 2007; Moore and Lien 2007). Improving predictive capability for these NLIWs through a better understanding of the variability of internal tide generation at the Luzon Strait is another motivation for this work. Park and Farmer (2013) recently showed that accounting for effects of the Kuroshio on wave propagation west of the strait

improves the prediction of NLIW timing, but predicting the amplitude is still a challenge.

The two ridges in the Luzon Strait contain multiple internal tide generation sites, and the resultant combination of waves produces interference patterns in depth-integrated energy fluxes (Figs. 1b,c). Energy flux vectors form a clockwise gyre in the northern section of the strait, where both the west and east ridges generate significant internal tides. To the south, where the western ridge is deeper and does not generate strong internal tides, energy fluxes emerge primarily from the east ridge, consistent with a single source there. These patterns are predicted in models (Jan et al. 2008; Buijsman et al. 2012) and confirmed in

measurements made during the IWISE pilot cruise (Alford et al. 2011).

The main goal of this work is to quantify influences from the mesoscale or Kuroshio using the coherence of internal tides over several spring–neap cycles. The coherent portion of the internal tide maintains a constant phase and amplitude with respect to the barotropic tidal forcing. Quantifying the coherence of the internal tide is important for several reasons. Estimates of internal tide energy flux made from satellite altimetry only capture the coherent portion of the signal (Ray and Zaron 2011; Zhao 2014). Knowledge of the coherent–incoherent partitioning is needed to make accurate estimates of internal tide propagation and induced mixing or to remove the internal tide signal for investigation of other nontidal processes. Coherence is also closely related to the predictability of internal tides and associated NLIWs. If it were 100% coherent, the internal tide could be predicted given knowledge of the barotropic forcing and the (constant) amplitude and phase of each constituent. Several mechanisms could lead to the incoherence of the internal tide in the Luzon Strait. Although they are not necessarily independent, we will here divide them into a conceptual framework of "local" and "remote" mechanisms.

Local refers to processes occurring in the Luzon Strait, encompassing both ridges. First, generation at the ridges may be modified by changes in stratification or shear over those sites. The Kuroshio is the dominant source of variability in stratification and shear in the Luzon Strait. Generation at one ridge may also be modified by waves generated at the other ridge. Changes in phase speed between the ridges caused by the Kuroshio could alter the phase of those waves, leading to variability in generation through changes in the bottom perturbation pressure (Kelly and Nash 2010; Zilberman et al. 2011). Finally, it is possible that the 3D interference pattern in the northern portion of the strait (Buijsman et al. 2014) could be shifted by the Kuroshio, leading to variability and loss of coherence where large gradients exist.

Remote refers to mechanisms involving signals that come from outside of the Luzon Strait. A portion of the westward-propagating diurnal internal tide from the Luzon Strait is expected to reflect back from the continental shelf, while the semidiurnal internal tide is expected to propagate onshelf (Klymak et al. 2011). Mesoscale variability between the shelf and Luzon Strait could alter the phase of the returning signals, leading to lower coherence. Another remote source is the Mariana Arc, which generates strong semidiurnal internal tides that propagate westward to the Luzon Strait. These waves propagate through a region of strong mesoscale variability east of the Luzon Strait, so their phase upon arrival could be highly variable (Kerry et al. 2013).

In this paper, we characterize the internal tide structure and variability in the Luzon Strait over several spring–neap cycles, focusing on two moorings with nearly full-depth coverage over 50 days. Data, methods, and oceanographic context are presented in section 2. Results are presented in section 3, focusing on detailed measurements from two moorings. In section 4, the coherent and incoherent portions of the internal tide are separated. In section 5, we examine the coherence of the internal tide in the model and estimate the effect of several mechanisms on the internal tide coherence. A summary of the main conclusions is given in section 6.

2. Data

Observations were made during IWISE, a research initiative to study the generation, propagation, and dissipation of internal waves in the Luzon Strait. A pilot experiment was conducted during summer 2010, consisting of two short-term moorings and 19 shipboard LADCP/CTD stations (Alford et al. 2011) along a northern and southern line. During the summer of 2011, an eight-element moored array (Fig. 1) was deployed along the same northern and southern lines. The goal of the array was to occupy the same locations studied during the pilot for a longer period in order to measure the time variability of those signals over several spring–neap cycles. As a result of the challenging environment, not all moorings returned full-depth data. In this paper, we focus on two moorings (A1 and S9) where nearly full-depth measurements were obtained, allowing reliable separation of barotropic and baroclinic signals and calculation of internal tide energy and flux.

a. A1

Mooring A1 was located on the eastern ridge in the central Luzon Strait (20°31.4′N, 121°40.5′E) at a water depth of 1446 m. A "Stablemoor" platform at a depth of 705 m housed upward- and downward-looking, 75-kHz RDI Long Ranger acoustic Doppler current profilers (ADCPs), which measured velocity over depths of ~120–650 and ~725–1200 m with 5-min time resolution. An upward-looking 300-kHz ADCP at 80 m measured near-surface velocity. Seabird (SBE)-37 MicroCATs (temperature, salinity, and pressure) and SBE-56s (temperature) were deployed along the mooring with 2-min sampling rate. Pressure records from the SBE-37 MicroCATs were used to correct for mooring knockdown.

b. S9

Mooring S9 was located on the southern portion of the eastern ridge (19°18′N, 121°1.8′E) at a water depth of

2286 m. Two stacked McLane moored profilers (MPs) profiled depth ranges of 330–1260 and 1300–2220 m, measuring horizontal velocity, temperature, and salinity. The MP profiles at a nominal speed of 0.25 m s^{-1}, resulting in a complete profile approximately every hour. The MP has a vertical resolution of ~10 m for velocity and 2 m for density. A subsurface float at 300 m contained an upward-looking, 75-kHz ADCP that measured velocity from ~30 to 300 m. Between this float and a smaller float at 70 m, a T chain consisting of SBE-56 temperature loggers spaced 15 m apart measured temperature. Pressure records from the bottom and top of the T chain were used to correct the SBE-56 temperature records for mooring knockdown (see the appendix for details). Salinity was estimated for the T chain using the observed T–S relation from the SBE-37. For the following analysis, all data from both moorings were interpolated onto a uniform grid with 10-m vertical and 1.5-h temporal spacing.

c. Models

We also make use of two numerical models in this analysis. The first is the Massachusetts Institute of Technology general circulation model (MITgcm) (Marshall et al. 1997), which uses more detailed bathymetry and provides higher spatial resolution but does not contain any mesoscale variability. The second is the Luzon Strait Ocean Nowcast/Forecast System (LZSNFS, hereinafter LZS) model, which has coarser resolution but is run over a longer time period and contains a realistic Kuroshio and mesoscale variability in addition to tidal forcing.

1) MITgcm MODEL

MITgcm was used in 3D configuration, as described in Buijsman et al. (2014). The model uses realistic topography merged from high-resolution gridded multibeam data with a resolution of ~300-m and 30-arc-s resolution global topography/bathymetry grid (SRTM30_PLUS) data from the Smith and Sandwell database with a resolution of ~1 km (Smith and Sandwell 1997). The density stratification is horizontally uniform and derived from temperature and salinity data collected in between the ridges (Alford et al. 2011). The tidal forcing at the east, west, north, and south model boundaries is composed of barotropic velocities extracted from TOPEX/Poseidon, version 7.2 (TPXO7.2; Egbert and Erofeeva 2002).

2) LZS MODEL

The LZS model is an application of the NRL Ocean Nowcast/Forecast System (Ko et al. 2008). The system is an integration of a dynamical ocean model and a statistical data analysis model. The model derives its ocean bottom topography from the Digital Bathymetry Data Base with 2-min resolution. Open boundary conditions are derived from a larger-scale model for the entirety of the East Asian seas (Ko et al. 2009). The barotropic tidal currents of eight tidal constituents (K$_1$, O$_1$, P$_1$, Q$_1$, K$_2$, M$_2$, N$_2$, and S$_2$) are obtained from TPXO7.2 (Egbert and Erofeeva 2002). This model includes the reflection of the internal tide from the continental shelf to the west but does not contain remote internal tides from outside the domain, including the Mariana Arc. The LZS model has now been used in several studies of internal waves in the Luzon Strait and South China Sea (Chen et al. 2013; Ma et al. 2013).

3. Results

Our primary focus is the internal tide energy and energy flux. However, we first take a moment to present the basic data (Fig. 2) and velocity spectra (Fig. 3).

a. Basic signals

The nearly full-depth coverage allows us to unambiguously separate the barotropic and baroclinic signals. Barotropic tidal velocity is defined as

$$\mathbf{u}_{BT} = \frac{1}{H} \int_{-H}^{0} [\mathbf{u}(z,t)\, dz - \overline{\mathbf{u}}(z)]\, dz, \qquad (1)$$

where $\mathbf{u}(z, t)$ is the instantaneous velocity, and $\overline{\mathbf{u}}(z)$ is a slowly varying subtidal component. Baroclinic velocity is defined as

$$\mathbf{u}' = \mathbf{u}(z,t) - \mathbf{u}_{BT}. \qquad (2)$$

The spring–neap cycle of tidal forcing is evident in the barotropic velocity (Fig. 2a). The barotropic velocities are very strong, up to 0.48 m s^{-1} at A1, and 0.31 m s^{-1} at S9. Total velocities (Figs. 2b–d) are dominated by tidal frequency motions and a strong spring–neap cycle as well as subtidal motions. Vertical displacements are tidally dominated and increase with depth, as indicated by the variability of density contours.

b. Spectra

Rotary spectra of baroclinic horizontal velocity at a depth of 250 m from S9 are presented in Fig. 3 (spectra from A1 are similar in character and are not shown). The spectra are dominated by peaks at tidal frequencies as well as sum and difference frequencies (e.g., M$_2$ + K$_1$) and higher harmonics. The spectra are elevated about 10–15 times above the theoretical Garrett–Munk (GM76) internal wave spectrum (Garrett and Munk
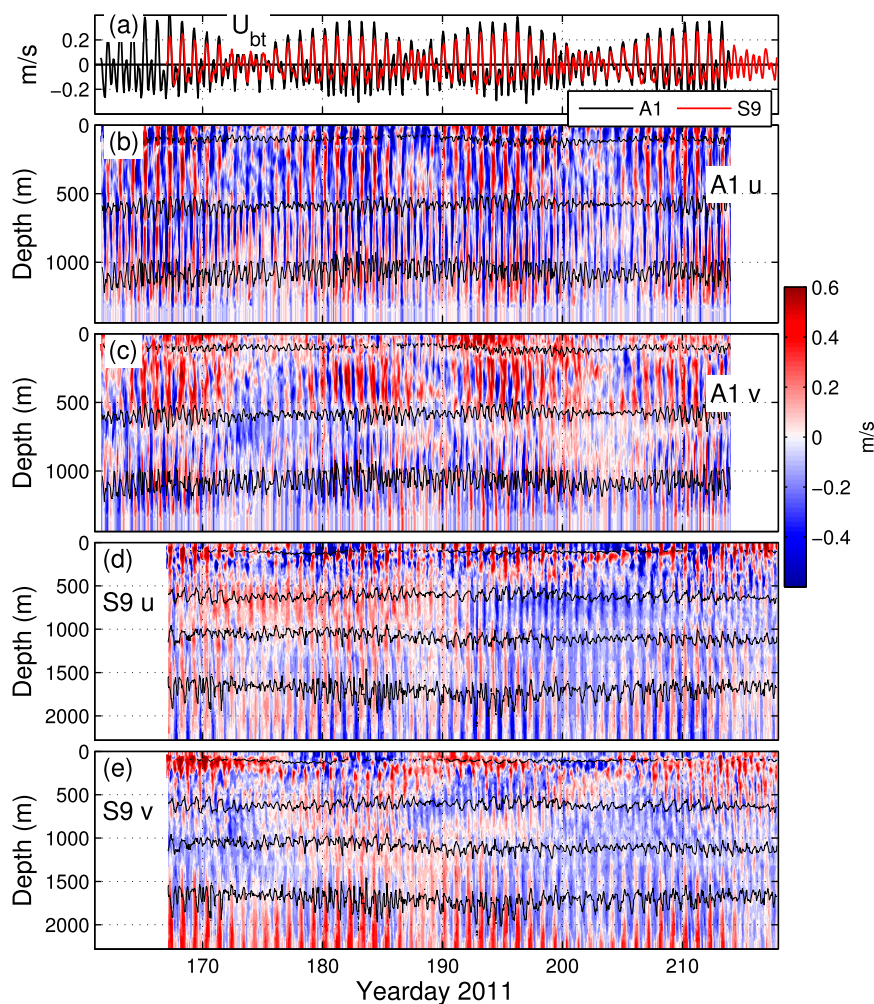
FIG. 2. Raw data from moorings A1 and S9. (a) Zonal component of barotropic velocity [Eq. (1)]. (b) A1 zonal velocity, (c) A1 meridional velocity, (d) S9 zonal velocity, and (e) S9 meridional velocity. Black lines are isopycnal contours at approximately 500-m intervals. Contour values (kg m^{-3}) are (1023.2, 1026.8, and 1027.4) for A1 and (1023.1, 1027.0, 1027.45, and 1027.6) for S9.

1972; Cairns and Williams 1976) but follow a similar slope and falloff with increasing frequency. The extreme elevation above GM levels nearly completely masks the usually prominent inertial peak, which here is only barely detectable.

c. Mesoscale velocity and Kuroshio

We use the large spatial extent of the mooring array and the LZS model to characterize the spatial and temporal structure of the Kuroshio and mesoscale velocity field during the experiment. Figure 4 shows low-passed (cutoff of 0.25 cpd) velocity vectors from moored ADCPs (color) at 150 m, with the color indicating the time of each measurement (only every 3 days are shown for clarity). Gray vectors are the time-mean low-passed velocity at 150 m from the LZS model during the

experiment, which are generally consistent with the low-pass filtered observations. A persistent Kuroshio intrusion was present during the experiment, entering the Luzon Strait from the southeast and passing over the western half of the strait near the northern line before exiting to the east of Taiwan. It can be seen in observations at moorings N2 and MPN, where low-frequency velocity was strong and to the north during the experiment. Note that A1 was not in the path of the Kuroshio intrusion, which appears to be deflected around the island and shallow topography to the southeast of the mooring. Velocity measured at moorings along the southern line was also outside of the main Kuroshio intrusion but exhibited strong, variable low-frequency flows, likely eddies spun off of the Kuroshio intrusion.
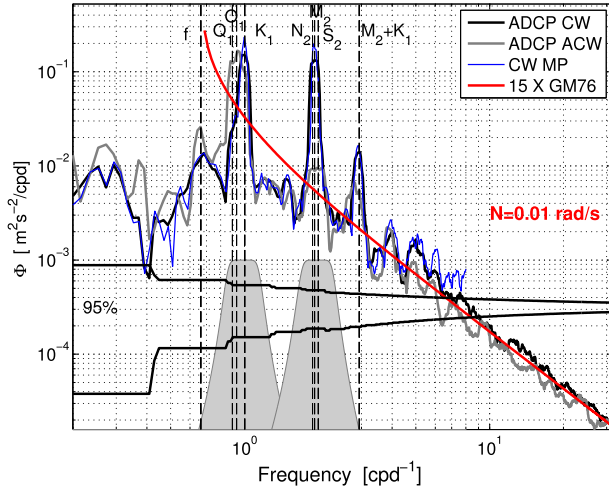
FIG. 3. Rotary spectrum of baroclinic velocity at 250 m at mooring S9. Spectra of the raw velocity measured by an upward-looking, 75-kHz ADCP are shown in black (clockwise) and gray (anticlockwise). The clockwise spectrum of the gridded MP velocity is plotted in blue. Gray shading shows the (scaled) frequency response of the bandpass filter used to isolate diurnal and semidiurnal frequencies. Red line is 15× the theoretical GM76 spectrum for the mean N at that depth. Black lines at bottom of figure indicate the 95% confidence limits.
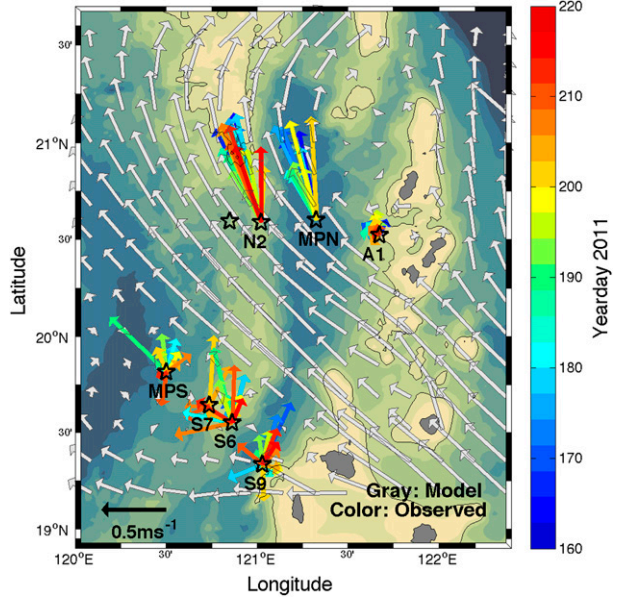

FIG. 4. Low-frequency velocity across the Luzon Strait during the experiment. Colored vectors show low-pass filtered velocities at 150 m from the mooring array. Gray vectors are time-mean velocity vectors at 150 m from the LZS model during the experiment.

Low-frequency velocity and stratification at S9 and A1 are computed by low-pass filtering with a cutoff of 0.25 cpd (Fig. 5). Both moorings have a stratification maximum near 150 m. In general N^2, defined as $(-g/\rho_o)(\partial\rho/\partial z)$, where g is the acceleration due to gravity, ρ is potential density, and ρ_o is a reference density, is higher at S9 than at A1. Variable N^2 is seen in the upper 200–300 m at both moorings. The low-frequency velocities are surface intensified at both moorings. The velocity at A1 appears to have a weak spring–neap cycle, likely because of the tidal rectification. The low-frequency velocity at S9 is dominated by strong $(0.5 \, \mathrm{m \, s^{-1}})$, near-surface (0–300 m) pulses with time scales of a few days.

d. Internal tides

Internal tide energy and energy flux are computed using standard methods (Kunze et al. 2002; Nash et al. 2005). The diurnal and semidiurnal frequency bands are separated by applying a bandpass filter (gray in Fig. 3) to the velocity and displacement data. The shallowest and deepest velocities are extended by linear extrapolation to the surface and bottom, respectively. Gaps in velocity were limited to the upper 20 m and lower 100 m at A1, and the upper 40 m and lower 50 m at S9. Stratification N^2 and vertical displacement η are linearly interpolated from the shallowest (deepest) measured value to zero at the surface (bottom). Gaps in displacement were limited

to the upper 70 m and lower 45 m at A1 and the upper 90 m and lower 60 m at S9. Smaller gaps in velocity and displacement in the middle of the water column are filled by linear interpolation.

Horizontal kinetic energy (HKE) and available potential energy (APE) are computed as

$$\mathrm{HKE} = \frac{1}{2}\rho\langle u'^2 + v'^2 \rangle, \quad \mathrm{and} \tag{3}$$

$$\mathrm{APE} = \frac{1}{2}\rho N^2 \langle \eta^2 \rangle, \tag{4}$$

where η is vertical displacement computed over 3-day windows and brackets indicate averaging over a wave period.

The perturbation pressure p' is computed as

$$p' = p_{\mathrm{surf}} + \int_z^0 \rho' g \, dz, \tag{5}$$

where the density perturbation is given as

$$\rho' = \frac{\overline{\rho}}{g}\overline{N}^2\eta. \tag{6}$$

The surface pressure p_{surf} is not measured but can be inferred from the baroclinicity condition that the depth-averaged pressure perturbation must vanish (Althaus et al. 2003):
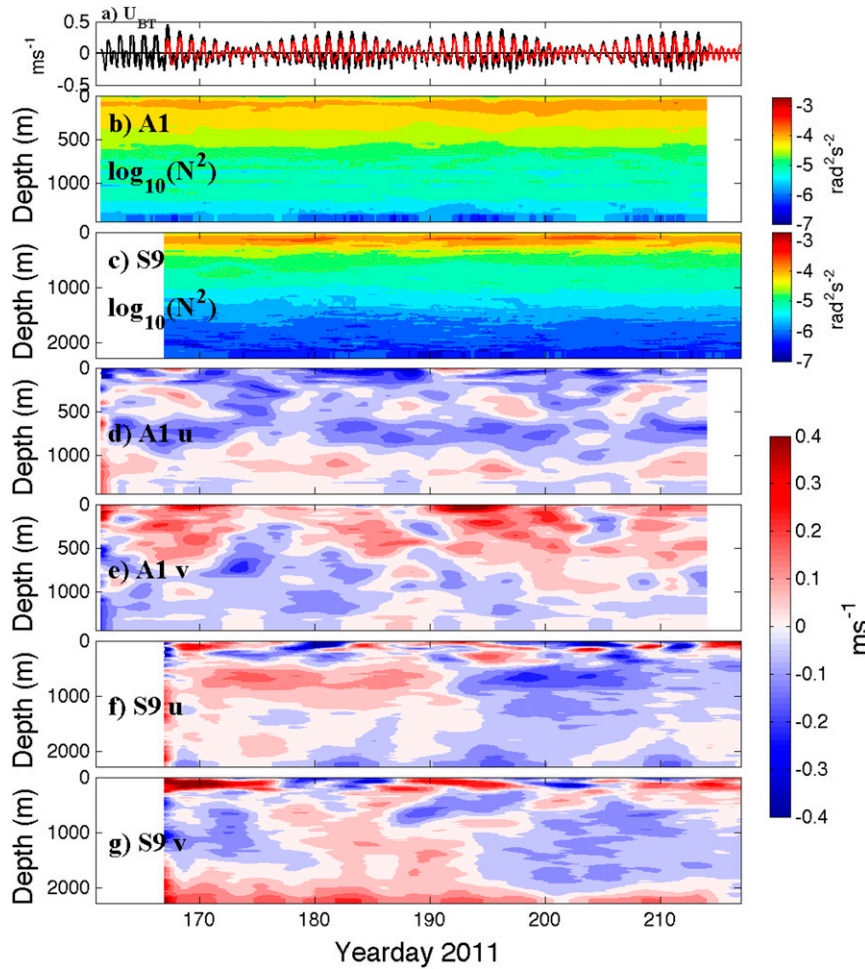
FIG. 5. Low-pass filtered stratification and velocity (4-day cutoff) at S9 and A1. (a) Zonal barotropic velocity at S9 (red) and A1 (black). (b) Stratification at A1. (c) Stratification at S9. (d) Zonal velocity at A1. (e) Meridional velocity at A1. (f) Zonal velocity at S9. (g) Meridional velocity at S9.

$$\frac{1}{H} \int_{-H}^{0} p'(z, t) \, dz = 0. \tag{7}$$

Determining p_{surf} and p' requires integrating over the full water depth. Thus, vertical gaps in measurements can introduce errors in this quantity (Nash et al. 2005; Rainville and Pinkel 2006). Sensitivity studies showed that errors in p_{surf} and p' because of the interpolating surface gaps were small ($<10\%$), allowing us to compute accurate profiles of p' over the depth ranges we sampled.

Energy flux is defined as the covariance of velocity and pressure perturbations:

$$\mathbf{F} = \langle \mathbf{u}' p' \rangle. \tag{8}$$

Although profiles of p' over the measured depth range are accurate, the depth-integrated energy and flux magnitude may differ from the true value because of the vertical gaps. This difference depends on the depth profile of the energy flux, which is normally surface intensified. To estimate this error, we resampled MITgcm model data from the mooring locations and computed energy flux in the same manner as the observations. Errors from the true value were 1% and 17% for diurnal and semidiurnal at A1 and 5% and 9% for diurnal and semidiurnal fluxes at S9. Importantly, these errors give rise to largely time-independent biases that do not affect our present focus on the time-variable signals and their coherence.

We also compute barotropic to baroclinic conversion, defined as (Kelly and Nash 2010)

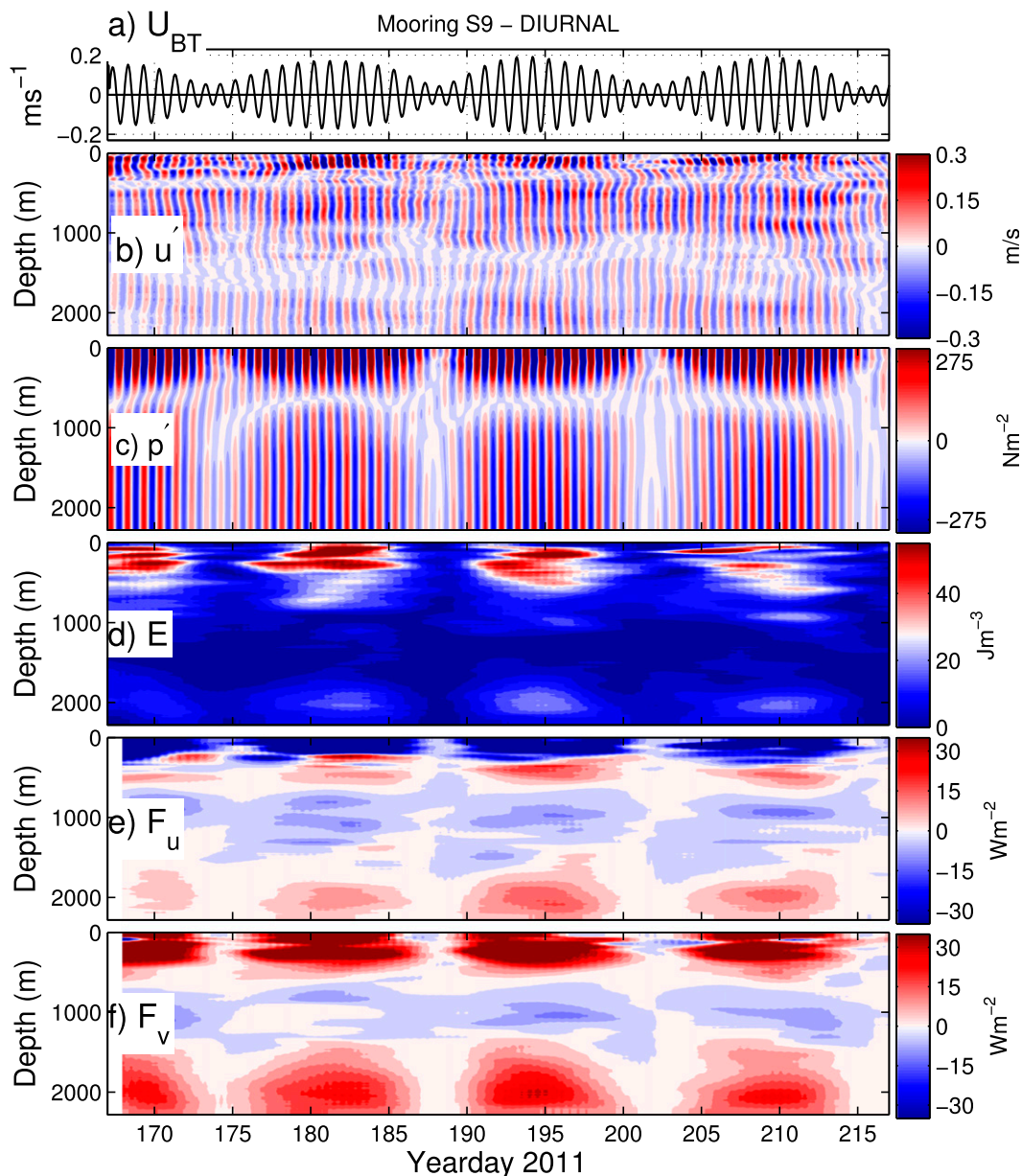$$C = \langle \nabla H \cdot (\mathbf{u}_{BT} p_b') \rangle, \tag{9}$$

FIG. 6. Diurnal internal tide quantities at S9: (a) barotropic velocity u_{BT}, (b) baroclinic zonal velocity, (c) perturbation pressure, (d) energy (HKE + APE), (e) zonal energy flux, and (f) meridional energy flux.

where ∇H is the bottom slope, p'_b is the perturbation pressure at the bottom, and brackets indicate averaging over a wave period.

e. Depth–time structure of internal tides

We first examine and contrast the depth–time structure of the diurnal internal tide at S9 and A1. Semidiurnal quantities are omitted for brevity; see the online supplemental material for figures. The diurnal signals are noticeably more coherent at S9, which we will further quantify in a future section. The diurnal

internal tide at S9 (Fig. 6) exhibits a relatively clean spring–neap cycle because of the beating of the K_1 and O_1 components. The vertical structure of perturbation pressure, energy, and flux appears to be low mode and is similar during each spring tide. Energy and flux are largest in the upper 500 m, with a smaller peak in the lower water column.

The diurnal velocity at A1 (Fig. 7b) also shows a strong spring–neap cycle. Energy (dominated here by HKE) has a similar vertical structure during all four spring tides. However, perturbation pressure (c) is more
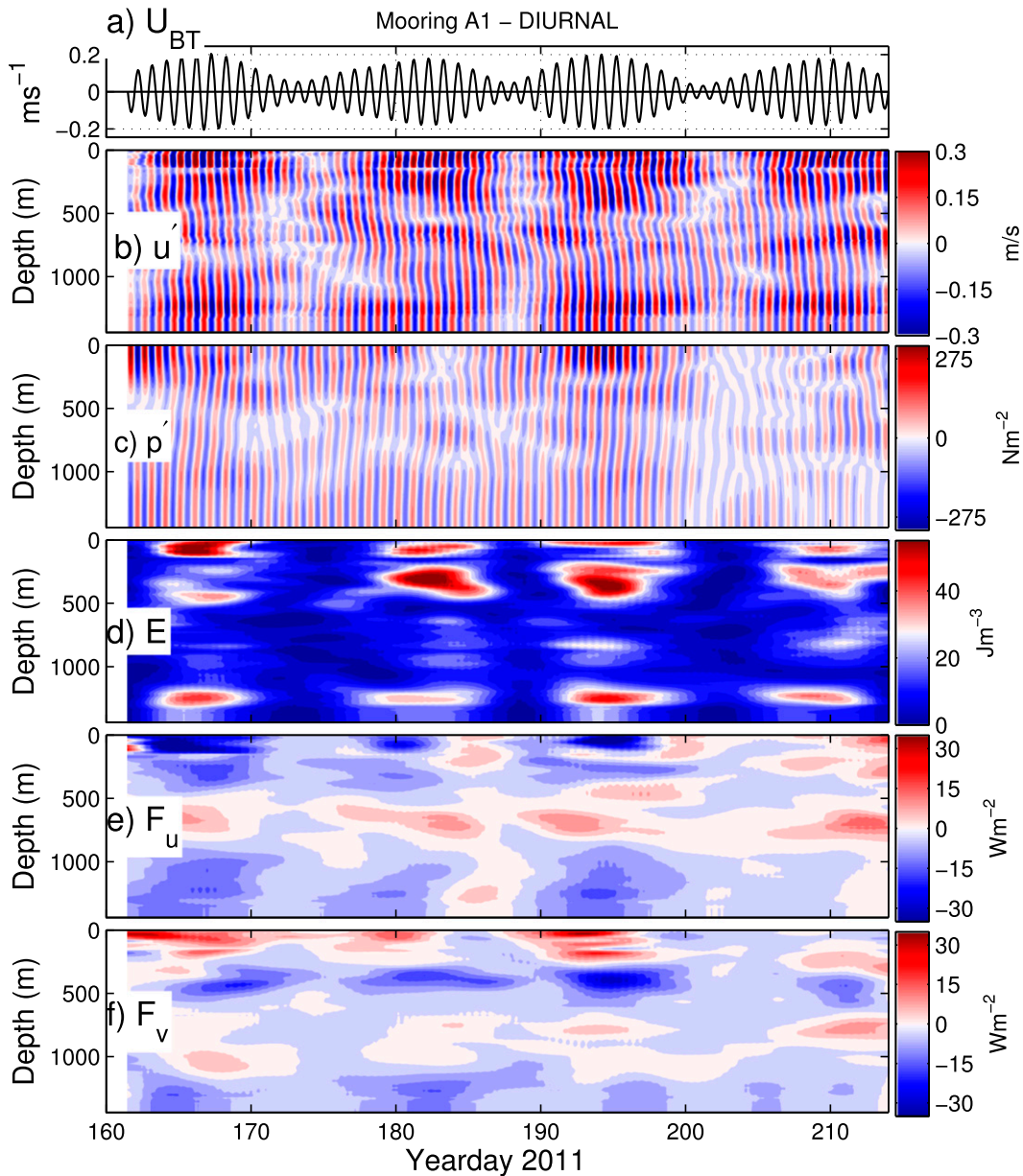
FIG. 7. As in Fig. 6, but for A1.

variable in both time and depth and does not have such an obvious spring–neap cycle. As a result, the depth and time structure of flux is more variable, notably during the last spring tide (yearday > 205). It will be shown in a later section that this lowers the coherence of the diurnal internal tide at A1.

f. Modal decomposition

The modal structure of the internal tide was also examined by fitting velocity and displacement profiles to mode shapes determined numerically from the IW vertical structure equation:

$$\frac{d^2}{dz^2}\phi(z) + \frac{N^2(z)}{c_n^2}\phi(z) = 0, \tag{10}$$

where ϕ is the vertical mode shape, and c_n is the eigenspeed. The modal distributions of time-averaged, depth-integrated APE, HKE, and energy flux at S9 and A1 are shown in Fig. 8. The modal distributions are red, with most of the variance contained in the first three modes. Energy flux is dominated by mode 1 with the exception of the diurnal internal tide at A1, where mode 1 is the largest but modes 2 and 3 make up a larger fraction of the total (as can be seen by the cumulative
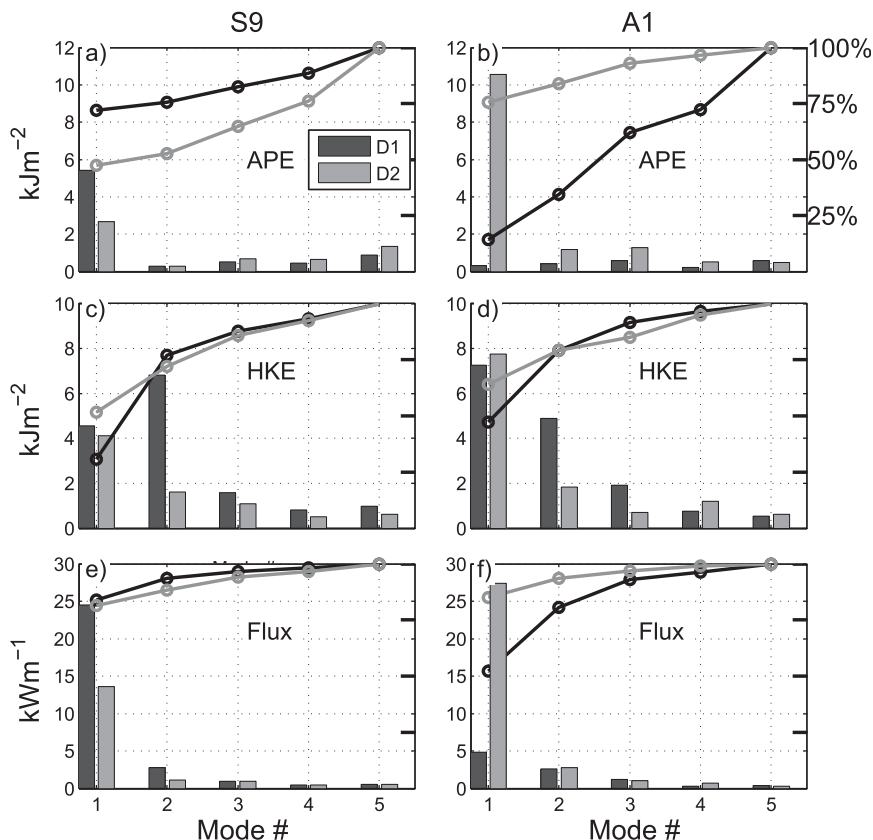
FIG. 8. Modal distribution of (top) APE, (middle) HKE, and (bottom) energy flux at (left) S9 and (right) A1. Lines with circles show the cumulative percent total, indicated by horizontal bars on right of axes and scale at upper right.

percent totals). The dominance of low-mode flux is typical of internal tides, since the pressure tends to act as a low-pass filter (Nash et al. 2005). HKE at both moorings has more variance at higher modes than energy flux but still tends to have a red spectrum, with about 75% of the total HKE contained in the first 2 modes. At S9, the mode-1 APE contains about 75% of the total in the diurnal band and less than 50% in the semidiurnal band. At A1, semidiurnal APE is dominated by mode-1 but diurnal APE is distributed more evenly among modes (note though that diurnal energy at A1 is dominated by HKE).

g. Depth-integrated internal tide energy and flux

Next, we examine time series of depth-integrated internal tide energy, energy flux, and conversion (Fig. 9). Time-mean quantities are summarized in Table 1. At S9, the diurnal barotropic forcing exceeds the semidiurnal forcing by about a factor of 2. This is reflected in the greater diurnal magnitude of energy (Fig. 9b), flux (Fig. 9c), and conversion (Fig. 9d) at S9.

At A1 (gray), diurnal and semidiurnal barotropic forcing have comparable magnitudes. Depth-integrated

energy is large in both bands, with semidiurnal exceeding diurnal most of the time. Note that the diurnal energy at A1 is dominated by HKE. While the diurnal and semidiurnal barotropic forcing and energy magnitudes are comparable, the energy flux and conversion are dominated by the semidiurnal band. The diurnal energy flux is small compared to the semidiurnal flux but still very large compared to typical open-ocean values. Semidiurnal flux appears to be well correlated with the barotropic forcing. Diurnal flux appears less correlated with barotropic forcing, even though the diurnal energy is large and well correlated.

A map view of the depth-integrated diurnal (left) and semidiurnal (right) energy fluxes at A1 (top) and S9 (bottom) is shown in Fig. 10. As also seen in Fig. 1, the observed and modeled fluxes generally show the same patterns, with an interference pattern to the north (Figs. 10a,b) and a single source to the south (Figs. 10c,d). The observed diurnal fluxes at A1 (Fig. 10a) show the greatest directional variability, with some of the fluxes toward the southwest in agreement with the model but also directed west and east at times. The semidiurnal
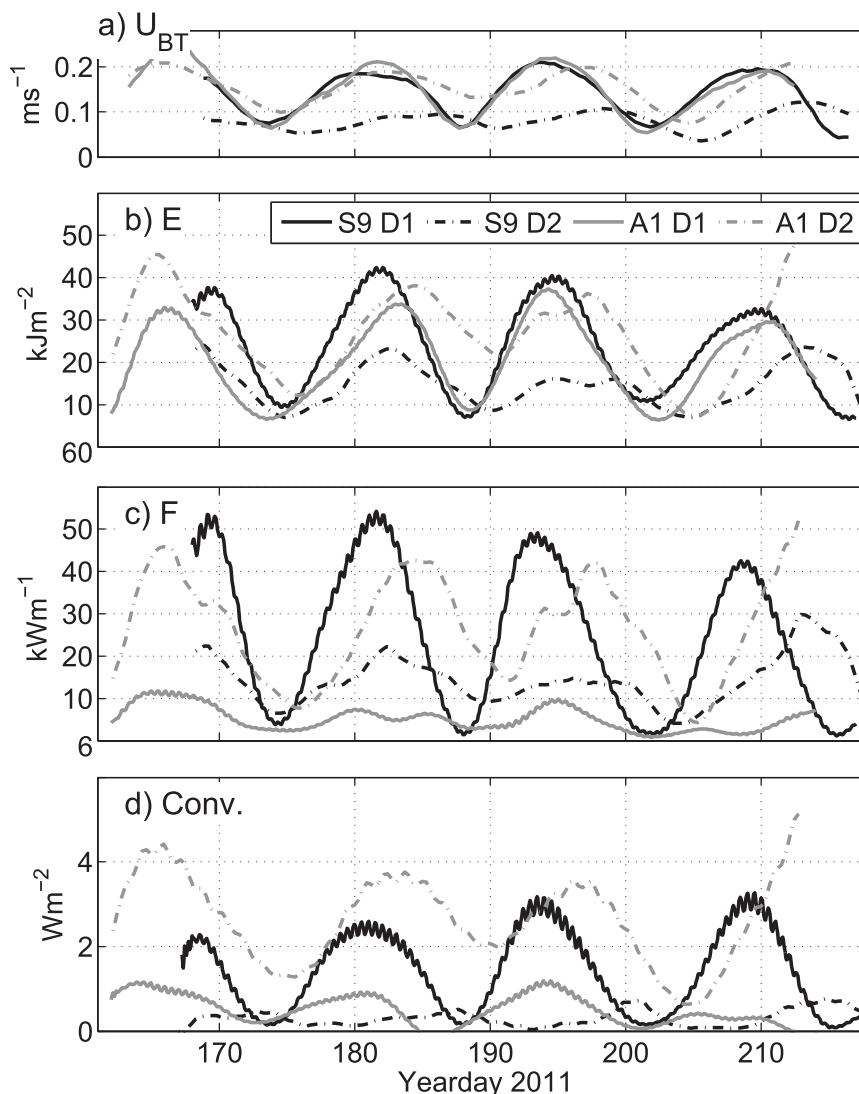
FIG. 9. Time series of depth-integrated internal tide quantities at moorings S9 (black) and A1 (gray). Diurnal quantities are shown with solid lines and semidiurnal are shown with dashed lines. (a) Barotropic velocity amplitude. (b) Depth-integrated energy (HKE + APE). (c) Depth-integrated energy flux magnitude. (d) Barotropic to baroclinic conversion.

band at S9 also shows more directional variability but less than the diurnal band at A1.

4. Coherent/incoherent separation

We next decompose the internal tide signals into coherent and incoherent components using a method similar to Nash et al. (2012). A harmonic fit to the major diurnal (K_1, O_1, and Q_1) or semidiurnal (M_2, S_2, and N_2) tidal constituents is performed on the bandpass-filtered time series of diurnal or semidiurnal velocity and pressure at each depth. Note that the bandwidth of the filter will affect the partitioning of coherent and incoherent

TABLE 1. Time-mean, depth-integrated energy, and energy flux for diurnal and semidiurnal internal tide at moorings S9 and A1. Direction is in degrees true (clockwise from north).

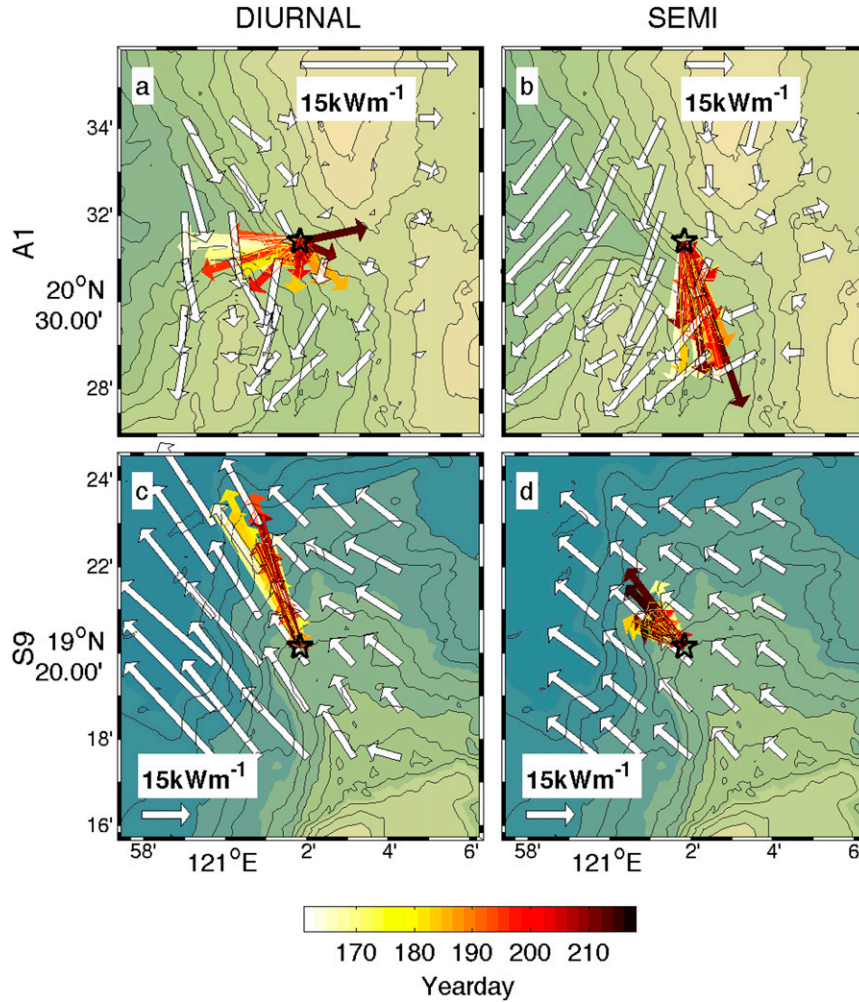|	Diurnal			Semidiurnal		
	$\overline{E}$ (kJ m^{-2})	$\overline{|F|}$ (kW m^{-1})	$\overline{\theta}$ (°True)	$\overline{E}$ (kJ m^{-2})	$\overline{|F|}$ (kW m^{-1})	$\overline{\theta}$ (°True)
S9	24	25	339	15	14	313
A1	21	5	236	27	27	169

DIURNAL   SEMI

FIG. 10. (left) Diurnal and (right) semidiurnal depth-integrated energy fluxes at moorings (top) A1 and (bottom) S9. White vectors are time-mean modeled (MITgcm) fluxes. Observed fluxes are colored by time.

signals (since an infinitely thin passband contains just one frequency and is 100% coherent by definition). The passbands we used (shown in gray in Fig. 3) are 0.85–1.15 cpd for the diurnal band and 1.7–2.3 cpd for the semidiurnal band, which include the three diurnal or semidiurnal constituents used for the harmonic fits. We do not include P_1 or K_2 in the fits because the record length is not long enough to resolve them from K_1 or S_2, respectively. The coherent part $(u, p)_c$ is defined as the reconstructed fit, and the remainder is defined as the incoherent part:

$$u_i = u - u_c, \tag{11}$$

$$v_i = v - v_c, \quad \text{and} \tag{12}$$

$$p_i = p - p_c. \tag{13}$$

Velocities are separated into barotropic and baroclinic components:

$$u'_c = u_c - u_c^{\text{BT}}, \quad \text{and} \tag{14}$$

$$u'_i = u_i - u_i^{\text{BT}}, \tag{15}$$

where $u_{c,i}^{\text{BT}}$ is the depth mean of $u_{c,i}$. Then baroclinic energy, energy flux, and conversion are computed separately for each component. In addition to the coherent and incoherent terms, there is a third component resulting from the cross terms. APE is given by

$$\text{APE} = \text{APE}_c + \text{APE}_i + \text{APE}_{\text{cr}}, \tag{16}$$

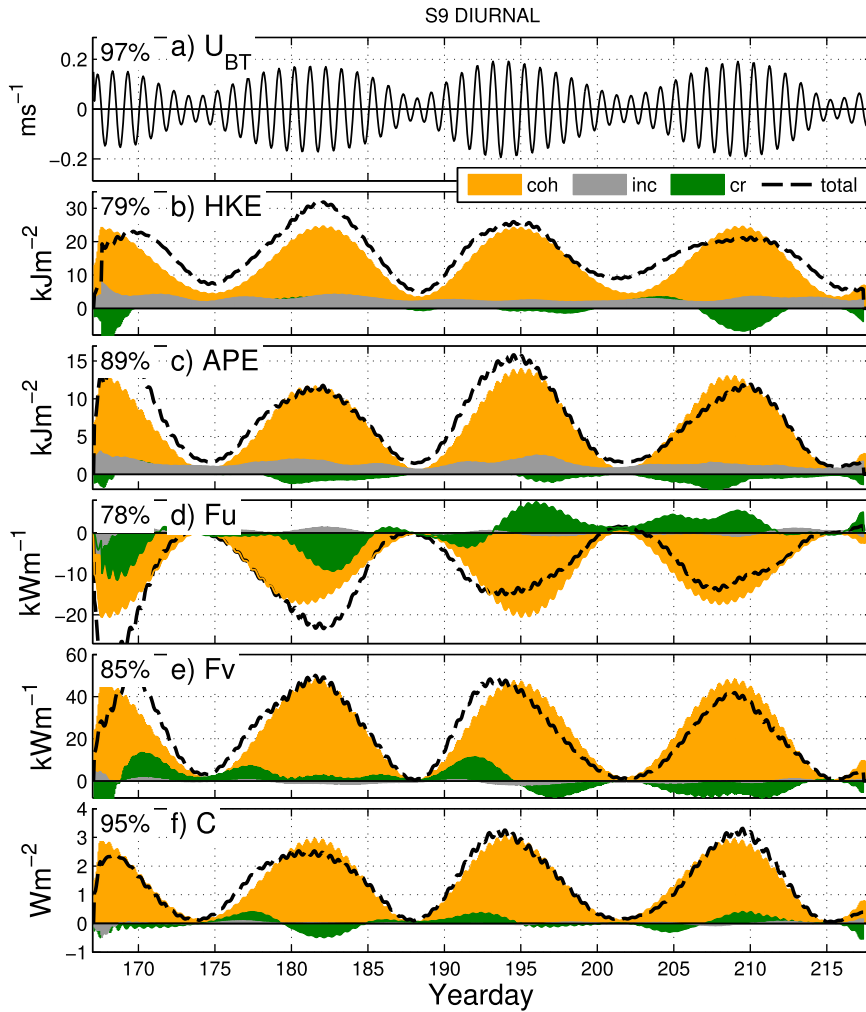$$\text{APE}_c = \frac{1}{2} \frac{g^2}{\rho N^2} \rho_c'^2, \tag{17}$$

FIG. 11. Results of coherent/incoherent separation for diurnal band at S9. (a) Zonal barotropic velocity. (b) HKE. (c) APE. (d) Zonal energy flux. (e) Meridional energy flux. (f) Conversion. Coherent, incoherent, and cross-term components are shown in color. Dashed black line shows the total of each quantity. Number in upper left of each panel indicates the percent of variance explained by coherent portion [Eq. (32)]. Note that the y-axis limits are not equal in Figs. 11–14.

$$\text{APE}_i = \frac{1}{2} \frac{g^2}{\rho N^2} \rho_i'^2, \quad \text{and} \qquad (18)$$

$$\text{APE}_{cr} = \frac{g^2}{\rho N^2} \rho_c' \rho_i'. \qquad (19)$$

HKE is given by

$$\text{HKE} = \text{HKE}_c + \text{HKE}_i + \text{HKE}_{cr}, \qquad (20)$$

$$\text{HKE}_c = \frac{1}{2} \rho \langle u_c'^2 + v_c'^2 \rangle, \qquad (21)$$

$$\text{HKE}_i = \frac{1}{2} \rho \langle u_i'^2 + v_i'^2 \rangle, \quad \text{and} \qquad (22)$$

$$\text{HKE}_{cr} = \rho \langle u_c' u_i' + v_c' v_i' \rangle. \qquad (23)$$

Energy flux is given by

$$F_u = F_c + F_i + F_{cr}, \qquad (24)$$

$$F_c = \langle u_c' p_c' \rangle, \qquad (25)$$

$$F_i = \langle u_i' p_i' \rangle, \quad \text{and} \qquad (26)$$

$$F_{cr} = \langle u_i' p_c' + u_c' p_i' \rangle, \qquad (27)$$

with similar expressions for the meridional component F_v. Barotropic to baroclinic conversion is given by
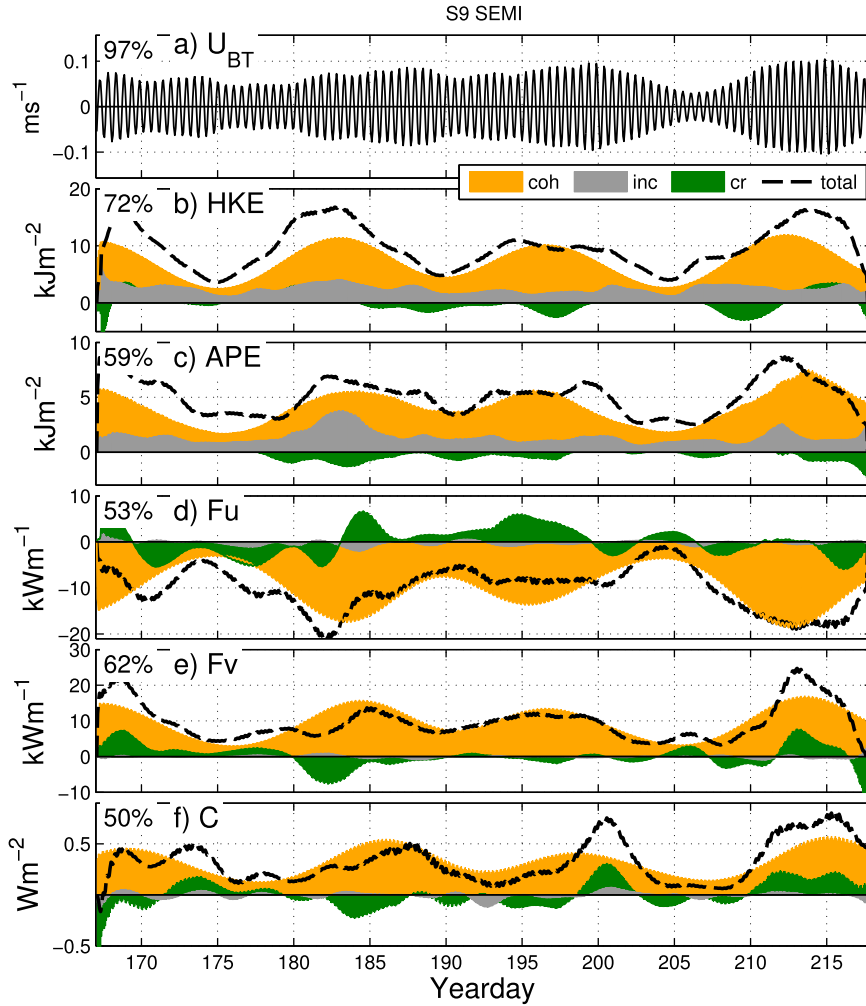
$$C = C_c + C_i + C_{cr}, \qquad (28)$$

FIG. 12. As in Fig. 11, but for the semidiurnal band at S9.

$$C_c = U_c^{\text{BT}} \cdot \nabla H p_c', \tag{29}$$

$$C_i = U_i^{\text{BT}} \cdot \nabla H p_i', \quad \text{and} \tag{30}$$

$$C_{\text{cr}} = U_c^{\text{BT}} \cdot \nabla H p_i' + U_i^{\text{BT}} \cdot \nabla H p_c'. \tag{31}$$

Results

As expected, because of their proximity to strong internal tide generation sites, the coherent term (Figs. 11–14, orange) is generally the largest of the three components. Although not strictly tied to the barotropic forcing, we loosely interpret the coherent component as the locally generated internal tide, in the absence of changes in mesoscale stratification or velocity. The magnitude and direction of the coherent flux vary according to the spring–neap cycle, and spring tides are not identical because of the Q_1 and N_2 components.

The remaining incoherent and cross terms are deviations from this regular cycle. They tend to also be the largest during spring tides, but their phase and/or amplitude vary on time scales shorter than the ~50-day record, and as a result they are not captured in the harmonic fits. Fits over individual spring tides (not shown) are more coherent, suggesting that changes in the internal tide's amplitude or phase occur on time scales between 14 and 50 days.

To compare the coherence at different locations, we compute the percent variance of each quantity that is explained by the coherent portion of the signal:

$$\%\text{var}_X = \left[1 - \frac{\text{var}(X - X_c)}{\text{var}(X)} \right] \times 100, \tag{32}$$

which is indicated in the upper left of each panel in Figs. 11–14 and Table 2.

The coherence of the diurnal (D1) energy flux at A1 is less than 30%, significantly less than the diurnal internal
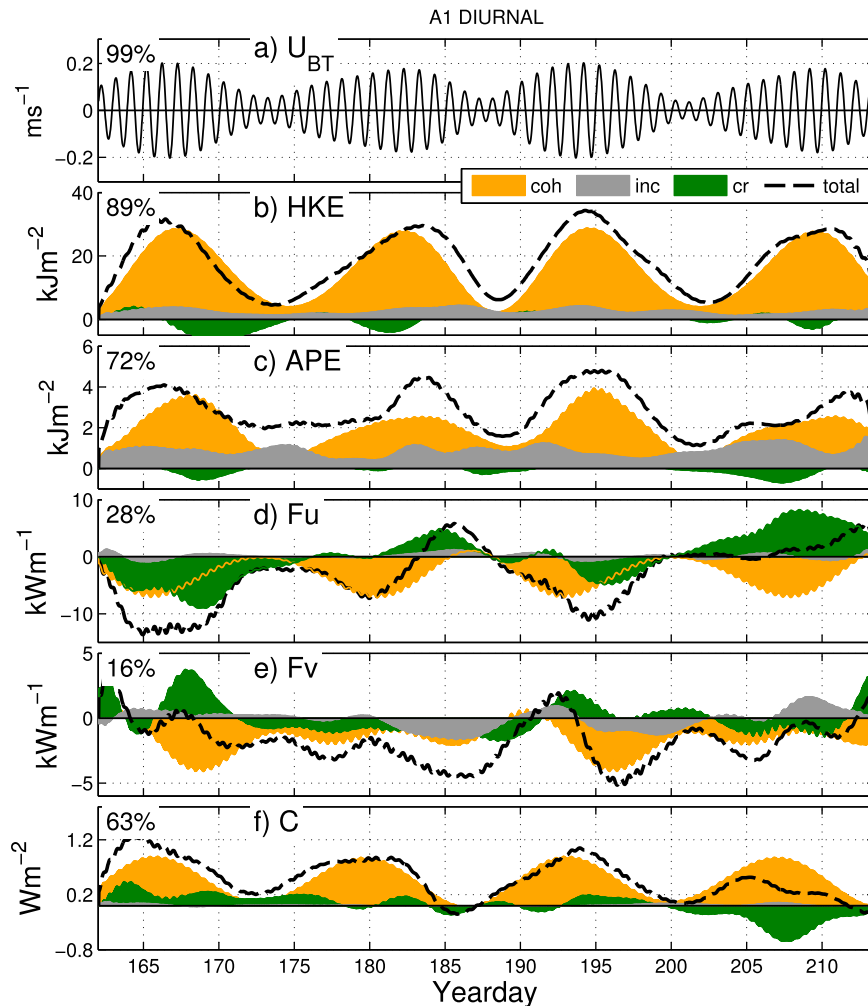
FIG. 13. As in Fig. 11, but for the diurnal band at A1.

tide at S9 and the semidiurnal (D2) internal tide at both locations. The diurnal A1 energy flux (Figs. 13d,e) is dominated by the cross-term fluxes, which are of comparable magnitude as the coherent fluxes and change the sign of both components of energy flux, resulting in highly variable energy flux vectors (as seen in Fig. 10). Further decomposing the cross-term fluxes into their two components [Eq. (27)] reveals that they are dominated by the term involving incoherent pressure $\langle u'_c p'_i \rangle$. This is consistent with the qualitative incoherent nature of perturbation pressure and energy flux seen in Fig. 7c. Conversion (Fig. 13f), which depends on the magnitude and phase of bottom perturbation pressure, is also less coherent at A1 (63%).

Cross-term fluxes in the semidiurnal band at A1 and both bands at S9 are of similar magnitude but smaller relative to coherent fluxes. At S9, the diurnal zonal F_{cr} (Fig. 11d) is negative during the first two springs and positive during the last two springs. Meridional F_{cr} is mostly positive during the first two springs, and negative

during the last two springs. The zonal F_{cr} appears to be somewhat correlated with the mean low-frequency velocity over the upper 1000 m (Fig. 5e), suggesting that the internal tide energy flux may be modified by the low-frequency eddy/mesoscale velocities.

The levels of coherence are summarized in Fig. 15, in which it can be seen that the diurnal band at S9 and the semidiurnal band at A1 are largely coherent (>70% for all quantities). Semidiurnal motions at S9 are slightly less coherent (>60%). Diurnal motions at A1 stand out as significantly less coherent (<30%, except for HKE) than the other three, consistent with the visual appearance of pressure (Fig. 7c) and the obvious veering of the flux direction (Fig. 10a). We discuss reasons for this next.

5. Discussion

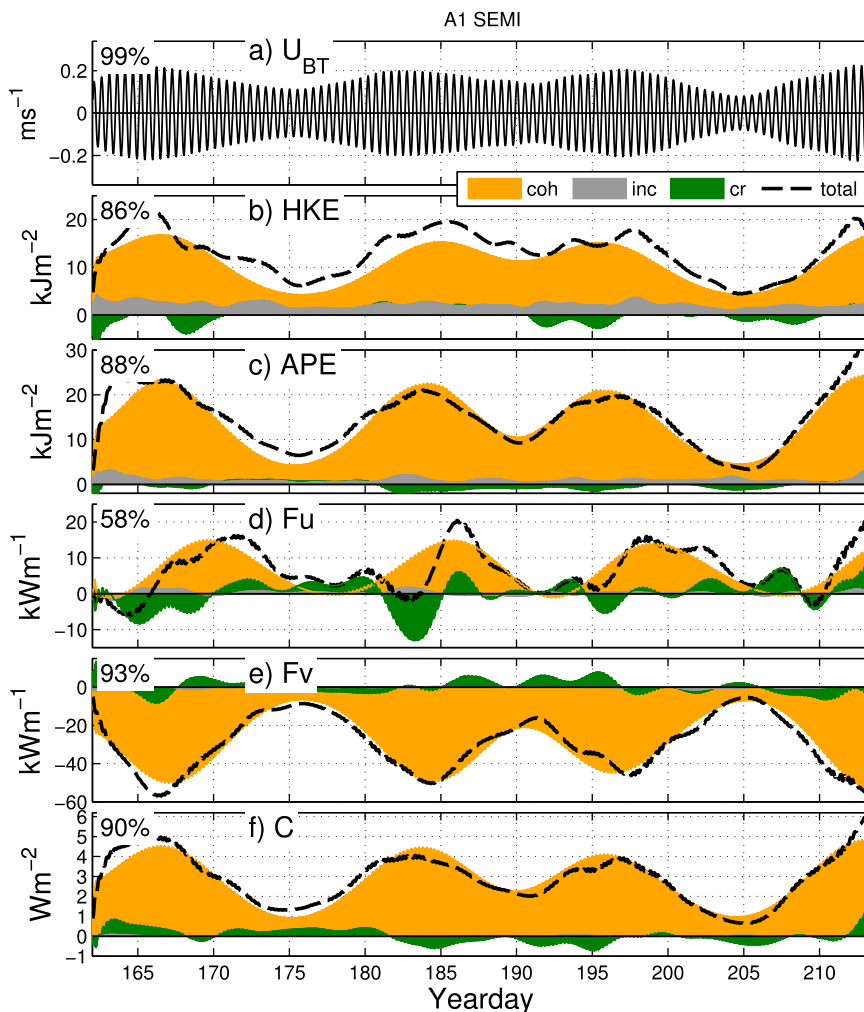Which of the several possible physical mechanisms are responsible for the observed levels of internal tide

FIG. 14. As in Fig. 13, but for the semidiurnal band at A1.

incoherence in the Luzon Strait? We first use a simple 2D model to estimate the effect variable stratification and velocity due to the Kuroshio has on internal tides propagating between the ridges at 20.5°N. The model consists of a coherent mode-1 internal tide generated at both ridges, with the total observed internal tide at A1 then consisting of the superposition of the locally generated wave (the observed coherent internal tide) and the wave arriving from the western ridge after traveling through variable phase speed between the ridges. The phase speed is calculated from the Taylor–Goldstein equation using low-passed velocity and stratification from the LZS model. The resulting coherence of flux and conversion in both bands [Eq. (32)] is 99%, showing that this mechanism has a negligible effect.

Next, we use a similar model to consider the impact of the diurnal internal tide reflected from the continental shelf to the west. In this scenario, a local

(coherent) internal tide is generated at A1 and propagates west to the slope at 117.5°E, where ⅓ of the energy reflects back, consistent with Klymak et al. (2011). The resulting diurnal coherence in this 2D model is 86% for flux and 99% for conversion. This mechanism could explain some of the lower diurnal coherence in flux at A1, but the observed coherence is significantly lower. However, it is enough to explain the 88% coherence of the diurnal flux at S9. Klymak

TABLE 2. Percent variance of observed mode-1 energy, flux, and conversion explained by coherent portion at moorings A1 and S9.

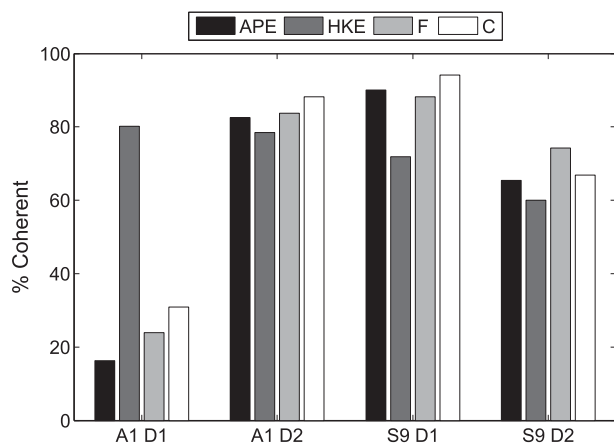|	APE	HKE	F_u	F_v	F	C
A1–D1	16	80	38	30	24	31
A1–D2	83	79	53	85	84	88
S9–D1	90	72	85	84	88	94
S9–D2	65	60	57	61	74	67

FIG. 15. Percent coherence of internal tides at A1 and S9 in both frequency bands, computed via Eq. (32).

et al. (2011) note that the amount of diurnal energy reflected is sensitive to the phase between mode-1 and mode-2 waves. Using the LZS model data, we calculated the mode-1 and mode-2 phase speeds, and the phase difference between them after propagating to the shelf (assuming they start in phase). The phase difference has a range of about 80°, suggesting that the fraction of energy reflected from the shelf could be quite variable in time, helping to explain the modest incoherence observed in the S9 diurnal internal tide.

Finally, we consider the effect of remote (semidiurnal) waves from the Mariana Arc. In recent modeling studies, Kerry et al. (2014) found that including remote waves from the Mariana Arc increased the variability of M_2 conversion at the Luzon Strait. We estimate the westward energy flux from the Mariana Arc as $1.3\,kW\,m^{-1}$ from Kerry et al. (2013), assuming a line source and no dissipation or spreading. This is ~4% of the mean semidiurnal coherent flux at A1 and is likely an upper bound. In the absence of detailed stratification or velocity information along the entire transect, we assume that the phase speed and travel time vary similarly to a LZS model point east of the ridges. The phase of the arriving wave has a range of more than 360°, and the coherence of the semidiurnal flux in this 2D model is 69%. This is lower than the observed semidiurnal coherence at both A1 (93%) and S9 (73%), so this mechanism could account for those values. The coherence of semidiurnal conversion at A1 in this model is 86%, close to the observed value of 88%.

Though these simple 2D calculations neglect possible feedbacks that could change conversion, and do not include any scattering or dissipation, they provide a rough

estimate of the possible magnitude of incoherence that these mechanisms could produce. The results suggest that the arrival of remote semidiurnal internal tides from the Mariana Arc could account for the observed semidiurnal incoherence at both A1 and S9 and that the reflection of the diurnal internal tide from the continental shelf could account for the observed level of diurnal incoherence at S9. However, the observed ~30% coherence of the diurnal internal tide at A1 cannot be explained by these simple 2D models.

To investigate further, we use the 3D LZS model and compute coherence in the same way as for the observations (Fig. 16). Coherence in both frequencies is lower along the eastern ridge, especially south of 20°N. The diurnal band (Fig. 16c) also has a region of low coherence extending to the northwest from the eastern ridge near 20.5°N. Both diurnal and semidiurnal internal tides are largely coherent in the area of S9. A1 is located in a region of low diurnal coherence and higher semidiurnal coherence. A zonal transect (Fig. 16a) through A1 at 20.5°N shows excellent agreement between model and observations. A transect through S9 (Fig. 16b) shows good agreement in the diurnal band and slightly higher than observed coherence in the semidiurnal band. Since the model reproduces the observed patterns, we can use it to explore mechanisms for lowering coherence. Notably, since the model does not include remote waves from the Mariana Arc, more local effects appear responsible.

A clue to the diurnal incoherence at A1 is given in Buijsman et al. (2014), who identified a large gradient in the phase of mode-1 diurnal pressure at that location. We hypothesize that incoherence arises as the variable Kuroshio and mesoscale shifts this pattern back and forth, which Buijsman et al. (2014) were not able to examine since the MITgcm model did not contain mesoscale forcing. Here, we compute the phase of mode-1 perturbation pressure from the LZS model using a sliding harmonic fit to the diurnal and semidiurnal frequencies in overlapping 3-day windows. The diurnal phase (Figs. 17b,e) has a large gradient that runs from northwest to southeast, passing near A1 before continuing south along the eastern ridge. This pattern and strong north–south gradient between the ridges is similar to that seen in Buijsman et al. (2014) but appears to be less zonal near 20.5°N, possibly because of the addition of the Kuroshio in the LZS model. The gradient of the semidiurnal phase (Figs. 17c,f) is smaller at A1, in agreement with the higher coherence of that component. Near the location of S9, the gradient of diurnal phase is small and the semidiurnal phase gradient is larger, consistent with the relative levels of coherence observed there.
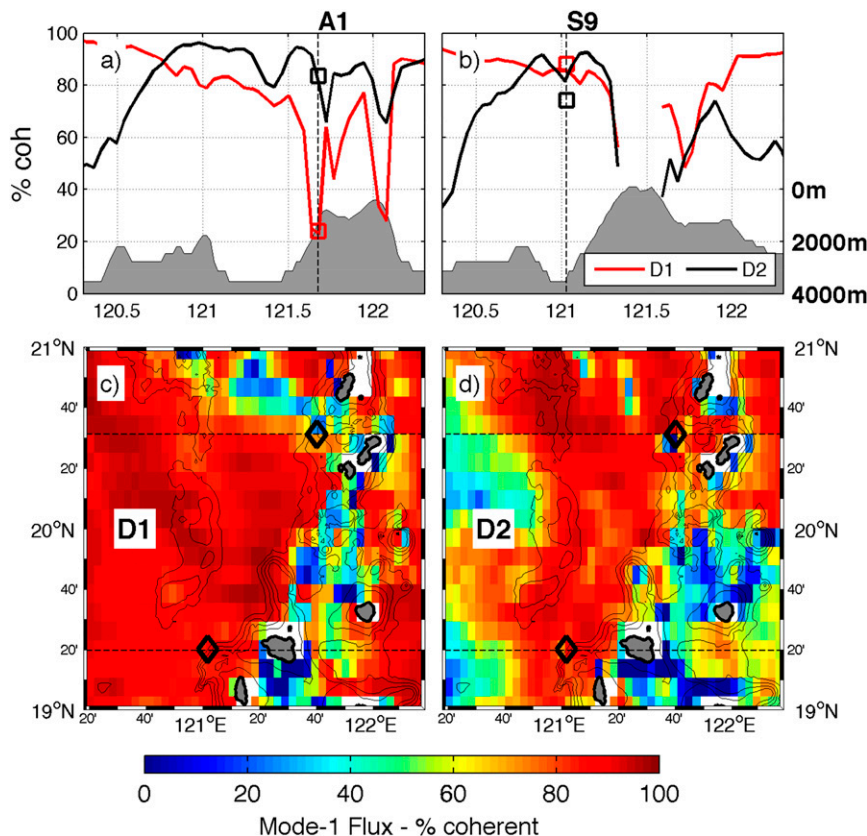
FIG. 16. Percent variance of the mode-1 energy flux explained by coherent component in LZS model for the (c) diurnal and (d) semidiurnal frequency bands. (top) Cross sections through (a) A1 and (b) S9, (bottom) with location indicated by dashed lines. Observed values from moorings are plotted as squares. Bathymetry along cross sections is shown in gray, with a scale at lower right of (b).

To test our hypothesis that shifting of this gradient is responsible for the lower coherence, we also examined the standard deviation of the baroclinic phase (not shown). It was generally largest where the largest gradients exist, consistent with this spatial pattern being advected or shifted laterally.

The shifting of the internal tide phase pattern must be caused by changes in stratification or velocity shear, which in the Luzon Strait are dominated by the intrusion of the Kuroshio. Figure 17 shows the low-frequency velocity at 100 m at two different times (Figs. 17a,d). In the first period (top row), there is a weaker, more diffuse Kuroshio, and the white diurnal phase contour passes through A1 (Fig. 17b). In the second time period (bottom row), the Kuroshio is stronger and more jetlike, and the diurnal phase pattern around A1 (Fig. 17e) appears to be shifted to the north. This suggests that the shifting of the diurnal pressure phase pattern is related to the low-frequency velocity or Kuroshio. However, the specifics of the interaction between the 3D internal tide response and

the background flows are complicated and beyond the scope of this paper.

6. Conclusions

The coherence and variability of internal tides in the Luzon Strait were studied using measurements from two moorings deployed for 50 days during the IWISE experiment. The observations reveal an extremely energetic internal wave field, with depth-integrated diurnal (semidiurnal) energy fluxes up to 54 (63) kW m^{-1}. Velocity spectra measured at the moorings were elevated up to 15 times above the theoretical GM spectrum (Fig. 3), likely because of energy input from strong internal tides and implying elevated turbulent mixing rates. The modal distribution of internal tide energy flux was red, with most of the flux contained in the first two modes.

The temporal variability of the internal tide is quantified by computing the coherent component, described by a sum of tidal frequencies with constant
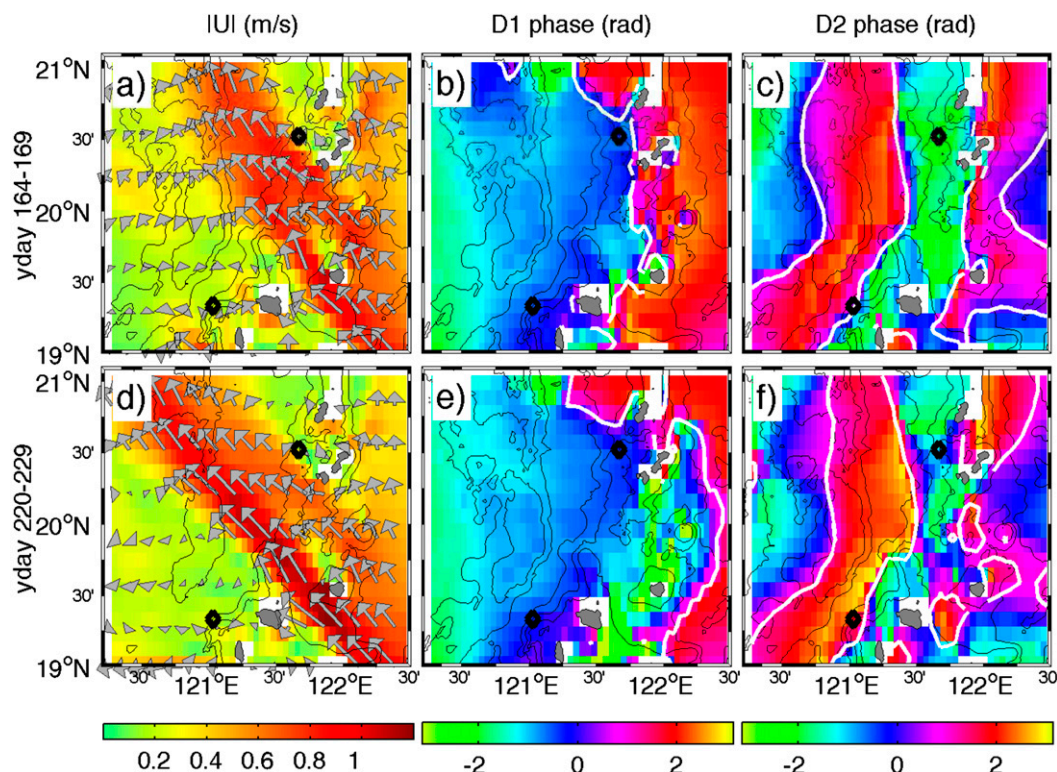
FIG. 17. (left) Low-frequency velocity at 100 m and phase of (middle) diurnal and (right) semidiurnal mode-1 pressure for (top and bottom) two time periods of the LZS model. The same phase value is contoured in white to show the shifting of the phase pattern. A constant offset is added to phases in the second time period to account for different barotropic phases.

amplitude and phase over the 50-day mooring deployment. The semidiurnal internal tide at A1 and both frequencies of internal tide at S9 were largely coherent (Table 2), with more than 70% percent of the energy flux variance explained by the coherent component. In contrast, the diurnal internal tide at A1 is significantly less coherent, with the coherent energy flux only 30% of the total. The phase and amplitude of diurnal perturbation pressure at A1 varies significantly over the mooring deployment, resulting in the low coherence.

Simple 2D calculations suggest that reflection of the diurnal internal tide from the continental shelf and remote semidiurnal internal tides arriving from the Mariana Arc could account for the observed levels of coherence, with the exception of the diurnal internal tide at A1. Instead, the much lower coherence of the diurnal internal tide at A1 is a result of the mooring's location near a large gradient in the 3D pattern of the baroclinic pressure phase. The LZS model, which contains a realistic Kuroshio and mesoscale variability, shows that changes in the Kuroshio intrusion into the Luzon Strait occur at the same time as shifts of the internal tide phase pattern in the Luzon Strait.

However, the multiple sources and 3D nature of the interference pattern makes it difficult to isolate the details of this mechanism. Continued progress will require a combination of data from many different observation platforms, combined with models such as the LZS that include the Kuroshio and mesoscale variability.
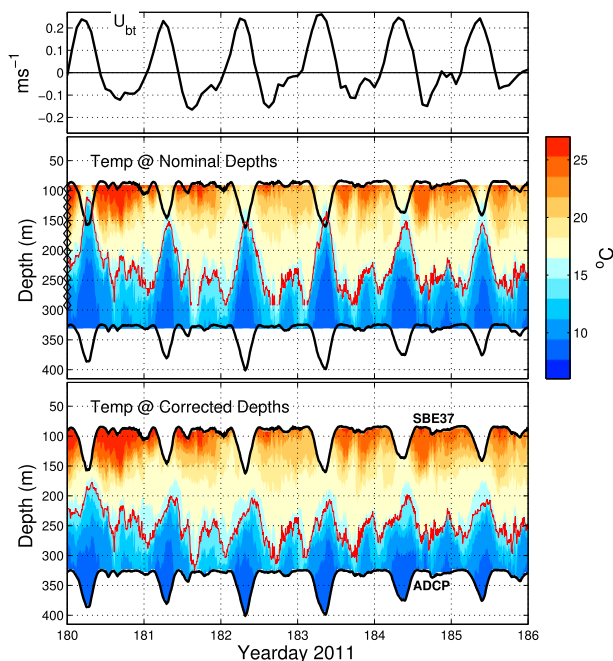
FIG. A1. Figure illustrating the removal of mooring blowdown from *T*-chain measurements at S9 and the effect on calculated vertical displacement. (a) Zonal barotropic velocity. (b) Thermistor string temperature plotted vs nominal depth of instruments. Black lines indicate depth of SBE-37 and ADCP at top and bottom of the *T* chain, respectively. (c) Temperature corrected for mooring blowdown using pressure measured at top and bottom of the *T* chain. The 15°C isotherm is contoured in red in (b) and (c) to illustrate the effect of blowdowns on inferred vertical displacement.

APPENDIX

Estimating Internal Wave Displacement from Temperature Chain Measurements with Mooring Knockdown

Extremely strong upper-ocean currents in the Luzon Strait inhibited moored profilers from climbing at times during the pilot experiment. To prevent this issue during the main experiment, mooring S9 was redesigned with an upward-looking ADCP and a temperature chain to measure the upper 300 m. The *T* chain consisted of SBE-56 temperature loggers spaced about 15 m apart, with an upward-looking ADCP at the bottom of the *T* chain and a SBE-37 MicroCAT at the top of the *T* chain. Here, we discuss the correction of mooring knockdown in these measurements.

Mooring knockdown, determined from pressure measured at the top (SBE-37) and bottom (ADCP) of the *T* chain, was up to ~75 m during strong flows at spring tide. The instantaneous depth of each SBE-56 temperature sensor was calculated from the pressure recorded at the top and bottom of the T chain, assuming that the T chain remained a straight line between the top and bottom. This assumption can be tested by comparing the difference in depth between the top and bottom (δz) to the known length of the wire $L = 237$ m. The maximum value of ($L - \delta z$) was about 10 m or about 4% of L, indicating that this is a good assumption. The cable could be slightly curved instead of in a straight line.

Figure A1 shows temperature plotted at the nominal depth of the *T*-chain instruments (Fig. A1a) and after interpolating to the actual depth (Fig. A1b). Without correction, large mooring blowdowns during spring tides (i.e., day 183) would be interpreted as extremely large vertical displacements. These vertical displacements have a large effect on the internal tide energy flux.

REFERENCES

Alford, M. H., and Coauthors, 2011: Energy flux and dissipation in Luzon Strait: Two tales of two ridges. *J. Phys. Oceanogr.,* **41,** 2211–2222, doi:10.1175/JPO-D-11-073.1.

——, and Coauthors, 2015: The formation and fate of internal waves in the South China Sea. *Nature,* in press.

Althaus, A., E. Kunze, and T. Sanford, 2003: Internal tide radiation from Mendocino Escarpment. *J. Phys. Oceanogr.,* **33,** 1510–1527, doi:10.1175/1520-0485(2003)033<1510:ITRFME>2.0.CO;2.

Buijsman, M. C., J. M. Klymak, and S. Legg, 2012: Double ridge internal tide interference and its effect on dissipation in Luzon Strait. *J. Phys. Oceanogr.,* **42,** 1337–1356, doi:10.1175/JPO-D-11-0210.1.

——, and Coauthors, 2014: Three-dimensional double-ridge internal tide resonance in Luzon Strait. *J. Phys. Oceanogr.,* **44,** 850–869, doi:10.1175/JPO-D-13-024.1.

Cairns, J. L., and G. O. Williams, 1976: Internal wave observations from a midwater float, 2. *J. Geophys. Res.,* **81,** 1943–1950, doi:10.1029/JC081i012p01943.

Chen, Y.-J., D. Shan Ko, and P.-T. Shaw, 2013: The generation and propagation of internal solitary waves in the South China Sea. *J. Geophys. Res. Oceans,* **118,** 6578–6589, doi:10.1002/2013JC009319.

Egbert, G., and S. Erofeeva, 2002: Efficient inverse modeling of barotropic ocean tides. *J. Atmos. Oceanic Technol.,* **19,** 183–204, doi:10.1175/1520-0426(2002)019<0183:EIMOBO>2.0.CO;2.

Farmer, D., Q. Li, and J.-H. Park, 2009: Internal wave observations in the South China Sea: The role of rotation and nonlinearity. *Atmos.–Ocean,* **47,** 267–280, doi:10.3137/OC313.2009.

Garrett, C., and W. Munk, 1972: Space-time scales of internal waves. *Geophys. Fluid Dyn.,* **3,** 225–264, doi:10.1080/03091927208236082.

Jan, S., R. Lien, and C. Ting, 2008: Numerical study of baroclinic tides in Luzon Strait. *J. Oceanogr.,* **64,** 789–802, doi:10.1007/s10872-008-0066-5.

Kelly, S., and J. D. Nash, 2010: Internal-tide generation and destruction by shoaling internal tides. *Geophys. Res. Lett.,* **37,** L23611, doi:10.1029/2010GL045598.

Kerry, C. G., B. S. Powell, and G. S. Carter, 2013: Effects of remote generation sites on model estimates of M2 internal tides in the Philippine Sea. *J. Phys. Oceanogr.,* **43,** 187–204, doi:10.1175/JPO-D-12-081.1.

——, ——, and ——, 2014: The impact of subtidal circulation on internal tide generation and propagation in the Philippine Sea. *J. Phys. Oceanogr.,* **44,** 1386–1405, doi:10.1175/JPO-D-13-0142.1.

Klymak, J. M., M. H. Alford, R. Pinkel, R. C. Lien, and Y. J. Yang, 2011: The breaking and scattering of the internal tide on a continental slope. *J. Phys. Oceanogr.,* **41,** 926–945, doi:10.1175/2010JPO4500.1.

Ko, D. S., P. J. Martin, C. D. Rowley, and R. H. Preller, 2008: A real-time coastal ocean prediction experiment for MREA04. *J. Mar. Syst.,* **69,** 17–28, doi:10.1016/j.jmarsys.2007.02.022.

——, S.-Y. Chao, P. Huang, and S. F. Lin, 2009: Anomalous upwelling in Nan Wan: July 2008. *Terr. Atmos. Oceanic Sci.,* **20,** 839–852, doi:10.3319/TAO.2008.11.25.01(Oc).

Kunze, E., L. Rosenfield, G. Carter, and M. C. Gregg, 2002: Internal waves in Monterey Submarine Canyon. *J. Phys. Oceanogr.,* **32,** 1890–1913, doi:10.1175/1520-0485(2002)032<1890:IWIMSC>2.0.CO;2.

Li, Q., and D. Farmer, 2011: The generation and evolution of nonlinear internal waves in the deep basin of the South China Sea. *J. Phys. Oceanogr.,* **41,** 1345–1363, doi:10.1175/2011JPO4587.1.

Lien, R.-C., F. Henyey, B. Ma, and Y.-J. Yang, 2014: Large-amplitude internal solitary waves observed in the northern South China Sea: Properties and energetics. *J. Phys. Oceanogr.,* **44,** 1095–1115, doi:10.1175/JPO-D-13-088.1.

Ma, B. B., R.-C. Lien, and D. S. Ko, 2013: The variability of internal tides in the northern South China Sea. *J. Oceanogr.,* **69,** 619–630, doi:10.1007/s10872-013-0198-0.

Marshall, J., A. Adcroft, C. Hill, L. Perelman, and C. Heisey, 1997: A finite-volume, incompressible Navier Stokes model for studies of the ocean on parallel computers. *J. Geophys. Res.,* **102,** 5753–5766, doi:10.1029/96JC02775.

Moore, S., and R.-C. Lien, 2007: Pilot whales follow internal solitary waves in the South China Sea. *Mar. Mamm. Sci.,* **23,** 193–196, doi:10.1111/j.1748-7692.2006.00086.x.

Munk, W., and C. Wunsch, 1998: Abyssal recipes II: Energetics of tidal and wind mixing. *Deep-Sea Res. I,* **45,** 1977–2010, doi:10.1016/S0967-0637(98)00070-3.

Nash, J. D., M. H. Alford, and E. Kunze, 2005: Estimating internal-wave energy fluxes in the ocean. *J. Atmos. Oceanic Technol.,* **22,** 1551–1570, doi:10.1175/JTECH1784.1.

——, S. M. Kelly, E. L. Shroyer, J. N. Moum, and T. F. Duda, 2012: The unpredictable nature of internal tides and nonlinear waves on the continental shelf. *J. Phys. Oceanogr.,* **42,** 1981–2000, doi:10.1175/JPO-D-12-028.1.

Park, J.-H., and D. M. Farmer, 2013: Effects of Kuroshio intrusions on nonlinear internal waves in the South China Sea during winter. *J. Geophys. Res. Oceans,* **118,** 7081–7094, doi:10.1002/2013JC008983.

Rainville, L., and R. Pinkel, 2006: Baroclinic energy flux at the Hawaiian Ridge: Observations from the R/P *FLIP. J. Phys. Oceanogr.,* **36,** 1104–1122, doi:10.1175/JPO2882.1.

Ramp, S. R., and Coauthors, 2004: Internal solitons in the northeastern South China Sea. Part I: Sources and deep water propagation. *IEEE J. Oceanic Eng.,* **29,** 1157–1181, doi:10.1109/JOE.2004.840839.

Ray, R., and E. Zaron, 2011: Non-stationary internal tides observed with satellite altimetry. *Geophys. Res. Lett.,* **38,** L17609, doi:10.1029/2011GL048617.

Simmons, H. L., R. W. Hallberg, and B. K. Arbic, 2004: Internal wave generation in a global baroclinic tide model. *Deep-Sea Res. II,* **51,** 3043–3068, doi:10.1016/j.dsr2.2004.09.015.

Smith, W. H. F., and D. T. Sandwell, 1997: Global sea floor topography from satellite altimetry and ship depth soundings. *Science,* **277,** 1957–1962, doi:10.1126/science.277.5334.1956.

Wang, Y. H., C. F. Dai, and Y. Y. Chen, 2007: Physical and ecological processes of internal waves on an isolated reef ecosystem in the South China Sea. *Geophys. Res. Lett.,* **34,** L18609, doi:10.1029/2007GL030658.

Zhao, Z., 2014: Internal tide radiation from the Luzon Strait. *J. Geophys. Res. Oceans,* **119,** 5434–5448, doi:10.1002/2014JC010014.

Zilberman, N. V., M. A. Merrifield, G. S. Carter, D. S. Luther, M. D. Levine, and T. J. Boyd, 2011: Incoherent nature of M_2 internal tides at the Hawaiian Ridge. *J. Phys. Oceanogr.,* **41,** 2021–2036, doi:10.1175/JPO-D-10-05009.1.